Counterion-assisted Adsorption strategy for High-Thermopower Thermo-electrochemical cell

Zhou Zhou, Shengming Zhang*, Xiangyang Qu, Qingxin Ge, Jiale Song, Tao Zhang, Rongliang Wu, Huaping Wang, Shiyan Chen*

State Key Laboratory of Advanced Fiber Materials, College of Materials Science and Engineering, Donghua University, Shanghai 201620, PR China

E-mail: smzhang@dhu.edu.cn, chensy@dhu.edu.cn

Table of content

Experimental Section

Chemicals:

Polyvinyl alcohol (PVA-124, 85000–124000, 99% hydrolyzed), dimethyl sulfoxide (DMSO), ethanol, Guanidine hydrochloride (GndCl), Methylguanidine hydrochloride (mGndCl), Potassium iodide (KI), Iodine (I_2), N-Isopropylacrylamide (NIPAM), N,N'-Methylenebisacrylamide (MBA), 2,2'-Azobis(2-methylpropionitrile) (AIBN) were purchased from Sinopharm Chemical Reagent Co. Ltd. and used without further purification. Graphite paper was used as an electrode.

Fabrication of PVA/PNIPAM hydrogel and TECs assembly:

3 g of NIPAM monomer, 10 mg of MBA, and 7 mg of AIBN were dissolved in DMSO at room temperature. The solution was purged with nitrogen for 10 minutes to remove dissolved oxygen, followed by polymerization at 70 °C for 6 h under sealed condition with stirring at 300 rpm. Subsequently, 3 g of PVA was added to the resulting solution and stirred at 120 °C for 2 h at 150 rpm to obtain the PVA/PNIPAM solution. The solution was cast into molds, frozen at −20 °C for 0.5 h, and then subjected to solvent exchange in ethanol for 6 h, during which the ethanol was replaced twice. The PVA/PNIPAM hydrogels were thoroughly washed with deionized water to remove residual solvents, yielding the final PNIPAM hydrogel. Hydrogel dimensions were measured using a vernier caliper.

The PVA/PNIPAM hydrogel was immersed in a 0.25 mM KI/KI_3 electrolyte solution at 4 °C for 12 h to achieve adsorption equilibrium. For Gnd^+-enhanced hydrogels, the required concentration of GndCl was added to the I^-/I_3^- lectrolyte. TECs were assembled using graphite paper as the working electrode.

Characterization:

UV–vis spectroscopy (UV-2600) equipped with a temperature controller was employed not only to monitor the phase separation temperature of the hydrogel but also to assess the relative concentration changes of I^- and I_3^- ions in the electrolyte at different temperatures, the phase transition temperature was determined from the change in absorbance at 500 nm during heating at a rate of 1 K min^{-1}. The method for calculating the actual I_3^- concentration in both the solution and hydrogel was detailed in Note 2. Fourier-transform infrared spectroscopy (FTIR) (Nicolet 6700) was used to qualitatively characterize the synthesis of PNIPAM, the interactions among hydrophobic groups during the temperature-responsive phase transition of the hydrogel, and the interaction between Gnd^+ and PNIPAM. Scanning electron microscopy (SEM) and energy-dispersive X-ray spectroscopy (EDS) (S4800) were employed to analyze the microstructure and elemental composition of the PVA/PNIPAM composite hydrogel. Micro-Raman spectroscopy (inVia-Reflex) was used to investigate changes in hydrophobic moieties within the PNIPAM hydrogel before and after the introduction of Gnd^+, to assess the effect of Gnd^+ on the solvation structure of I_3^- in the I^-/I_3^- electrolyte solution, and to monitor the concentration variation of I_3^- during the temperature cycling process (25–35–25 °C) in TECs. The mechanical properties of the PVA/PNIPAM hydrogel were tested using a tensile tester (Instron Model 5969), the tensile rate was set to 100 mm min^{-1}. The open-circuit voltage–time curves, current–voltage curves, output power curves of the TECs were measured using a chemical workstation (CHI660E). During the temperature-dependent CV measurements, graphite paper was used as the working electrode, a platinum sheet as the counter electrode, and an Ag/AgCl electrode as the reference electrode. Electrolyte solutions containing 0.25 mM I^-/I_3^- with either 40 mM KCl or 40 mM GndCl. The scan rate was set at 50 mV/s. To monitor the electrochemical behavior within the hydrogel, composite hydrogel electrodes were fabricated by embedding graphite paper into the gel matrix during the gelation process, which were then used as the working electrodes. The three-electrode cell was equilibrated at 25°C in a light-shielded water bath under ambient conditions, followed by pre-cycling to stabilize the CV curves. Rapid continuous CV scanning was then employed during the heating process to reduce interference in peak current analysis arising from potential I_3^- decomposition and volatilization during prolonged heating.

All-atom molecular dynamics:

Atomistic molecular dynamics simulations have been performed in the GROMACS [1] (version 2020.6) simulation package using the CHARMM 36 force field

[2] and the water molecules were modelled using the TIP3P water model. One polymer chain of 5 repeat unit was inserted into a cubic box of around 5 nm and then 30 I_3^- ions were also inserted into the same box. Two systems with 30 Gdm^+ and K^+ ions were separately inserted into the previous box and solvated with around 3200 water molecules. The counterions were inserted with random replacement of water molecules and thousands of steps of energy minimization were conducted. The equilibration of 5 ns was performed with restraints on the solute molecules to equilibrate the water molecules before the production runs of 20 ns. An integration time-step of 1 fs was used and the temperature was coupled to 303 K using the Nose-Hoover method and a cutoff scheme of 1.2 nm was used for the non-bonded interactions, and the Particle Mesh Ewald method [3] with a fourierspacing of 0.1 nm was applied for the long range electrostatic interactions. All covalent bonds with hydrogen atoms were constraint using the LINCS algorithm.[4] The presence of hydrogen bonds was calculated using the common criteria so that the maximum angle of the hydrogen-donor-acceptor was 30 degrees, and the distance between the acceptor and donor atoms was less than 0.35 nm.

Theoretical Analysis and Calculation

Note 1. Theoretical analysis of enhanced thermopower via increased constructed concentration gradient

In TECs that achieve thermoelectric conversion via the thermogalvanic effect of redox couples, the thermopower (also referred to as the Seebeck coefficient) can be expressed as[5]:

$$Se = \frac{E_H - E_C}{T_H - T_C} = \frac{\Delta E}{\Delta T}$$

where the subscripts “H” and “C” denote the hot and cold ends of the TECs, respectively.

According to the Nernst equation, for TECs governed by the reversible redox reaction aA+ne⁻ ↔ bB, the equilibrium potentials at the hot and cold sides can be expressed as:

$$E = E^0 + \frac{RT}{nF} ln \frac{(\alpha_A)^a}{(\alpha_B)^b}$$

where E^0 denotes the standard potential, α_A and α_B are the activities of species A and B, R is the ideal gas constant, and F is the Faraday constant. The activity (α_i) is defined as the product of the activity coefficient (γ_i) and the concentration (C)($\alpha_i = \gamma_i \times C$), *S2* can be further expressed as:

$$E = E^0 + \frac{RT}{nF}\left[ln\frac{(\gamma_A)^a}{(\gamma_B)^b} + ln\frac{(c_A)^a}{(c_B)^b} \right]$$

Therefore, the output voltage of the TECs, or equivalently the equilibrium potential difference ΔE, can be expressed as:

$$\Delta E = E_H - E_C = \frac{R}{nF}\left[ln\frac{(\gamma_A)_H^a}{(\gamma_B)_H^b} - ln\frac{(\gamma_A)_C^a}{(\gamma_B)_C^b} \right] + \frac{R}{nF}\left[ln\frac{(c_A)_H^a}{(c_B)_H^b} - ln\frac{(c_A)_C^a}{(c_B)_C^b} \right]$$

The term containing γ is governed by the solvation entropy difference of the redox ions (ΔS), whereas the latter term is controlled by the concentration gradient of the redox ions (ΔC) [6]. In this study, the thermovoltage contribution arising from redox-entropy effects is minor, while that from the concentration gradient predominates[7,8].

$$\frac{R}{nF}\left[ln\frac{(\gamma_A)_H^a}{(\gamma_B)_H^b} - ln\frac{(\gamma_A)_C^a}{(\gamma_B)_C^b} \right] \propto \Delta S$$

$$\frac{R}{nF}\left[ln\frac{(c_A)_H^a}{(c_B)_H^b} - ln\frac{(c_A)_C^a}{(c_B)_C^b} \right] \propto \Delta C$$

For the TECs dominated by $I_3^- + 2e^- \leftrightarrow 3I^-$, the contribution from the ΔC can be further expressed as:

$$\frac{R}{2F}\left[ln\frac{(c_{I_3^-})_H}{(c_{I^-})_H^3} - ln\frac{(c_{I_3^-})_C}{(c_{I^-})_C^3} \right] = \frac{R}{2F}\left[ln\frac{(c_{I_3^-})_H}{(c_{I_3^-})_C} - 3ln\frac{(c_{I^-})_H}{(c_{I^-})_C} \right]$$

In PVA/PNIPAM-based TECs, when the hot-side temperature exceeded the phase transition temperature, the concentration gradient of I_3^- within the TECs undergoes a significant alteration, resulting in the dominance of the ΔC contribution to the overall thermoelectric response.

$$\Delta E \propto \frac{R}{2F} ln\frac{(c_{I_3^-})_H}{(c_{I_3^-})_C}$$

By further enhancing the adsorption of I_3^- within the hydrophobic domains through a counterion-assisted strategy, an increased amount of I_3^- was adsorped and immobilized in the hydrophobic phase, resulting in a decreased free I_3^- concentration and thus promoting the generation of a higher ΔE.

Note 2. Electrochemical Analysis of Selective Ion Adsorption Processes

For diffusion-controlled reversible reactions, the peak current (i_p) in CV measurements can be described by the Randles-Sevcik equation as follows:

$$i_p = \left(2.69 \times 10^5\right) n^{\frac{3}{2}} A D^{\frac{1}{2}} C v^{\frac{1}{2}}$$

n is the number of electrons transferred per redox event, A is the electrode geometric area, D is the diffusion coefficient, C is the bulk concentration of the electroactive species, v is scan rate.

At a constant temperature, the peak current (i_p) of the diffusion-controlled oxidation reaction exhibits a linear relationship with the square root of the scan rate ($v^{1/2}$). The diffusion coefficient can thus be determined by fitting the linear plot:

$$D = \left[\frac{i_p}{\left(2.69 \times 10^5\right) n^{\frac{3}{2}} A D^{\frac{1}{2}} C v^{\frac{1}{2}}}\right]^2$$

The diffusion coefficient can also be described by the Stokes–Einstein equation：

$$D = \frac{k_B T}{6\pi\eta r}$$

Here, k_B is the Boltzmann constant, η is the solution viscosity, and is the hydrated or effective radius of the diffusing species. When two ions form tighter ion pairs or clusters, the effective radius r increases significantly, resulting in a decreased diffusion coefficient. Concurrently, the reduction in free ion concentration leads to a diminished peak current in CV measurements.

Note 3. Quantitative analysis of I_3^- adsorption behavior

According to the Lambert–Beer law, the absorbance (A) of a solution at a given wavelength is linearly proportional to the solute concentration (c) as expressed by：

$$A = \varepsilon l c$$

where ε is the molar extinction coefficient and l is the optical path length. Under fixed optical path and wavelength, remains constant, ensuring a linear relationship between absorbance and concentration.

The concentration of I_3^- in solution was calculated by establishing a linear calibration curve between concentration (mM) and UV-vis absorbance at 287 nm. The resulting concentration–absorbance relationship, based on different concentrations (c) and their corresponding absorbance values (x), can be expressed as:

$$c = \frac{(x + 0.6613)}{11.28565}$$

The actual ion concentration within the gel C_{gel}, was indirectly determined by immersing the ion-selective absorption gel in the electrolyte solution and measuring the decrease in the initial I_3^- concentration, in the solution. This relationship can be expressed as:

$$C_{gel} = \frac{\left(C_{sol}^{0} - C_{sol}\right)V_{sol}}{V_{gel}}$$

Where C_{sol}^{0} represents the initial concentration of I_3^- in the solution, C_{sol} denotes the residual concentration of I_3^- in the solution after adsorption by the PVA/PNIPAM gel, V_{sol} is the volume of the solution, and V_{gel} is the volume of the PVA/PNIPAM gel introduced into the electrolyte solution.

Figure and Table

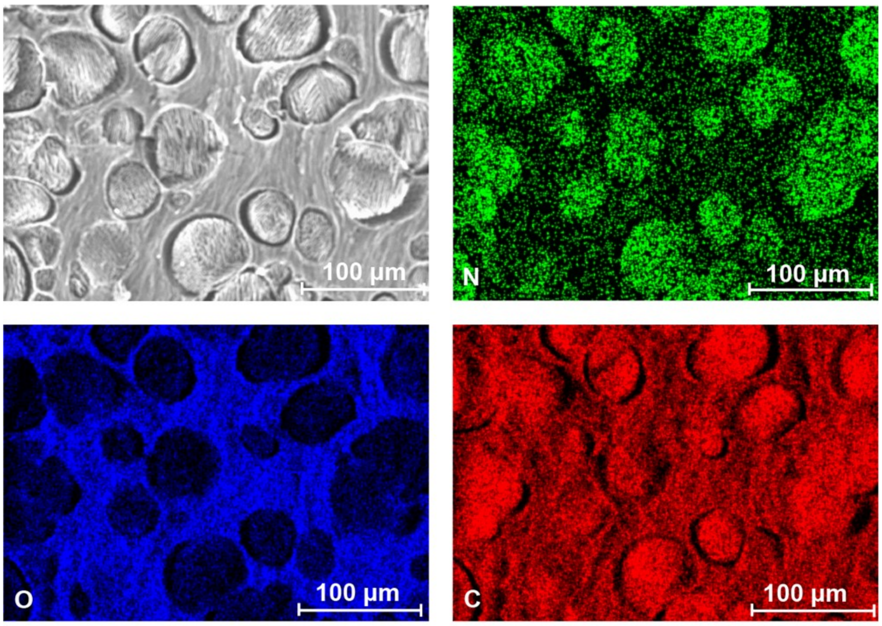

Figure S1. EDS mapping of PVA/PNIPAM hydrogel. The elements nitrogen (N), oxygen (O), and carbon (C) are represented by the colors green, blue, and red, respectively.

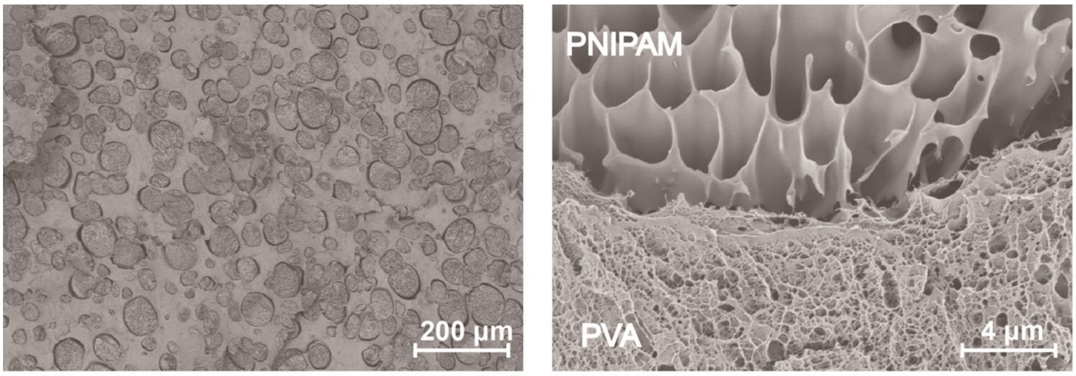

Figure S2. SEM images of PVA/PNIPAM hydrogel: micron-scale particulate domains correspond to PNIPAM (left). Regions with larger pore sizes correspond to PNIPAM, while dense pore structures correspond to PVA (right).

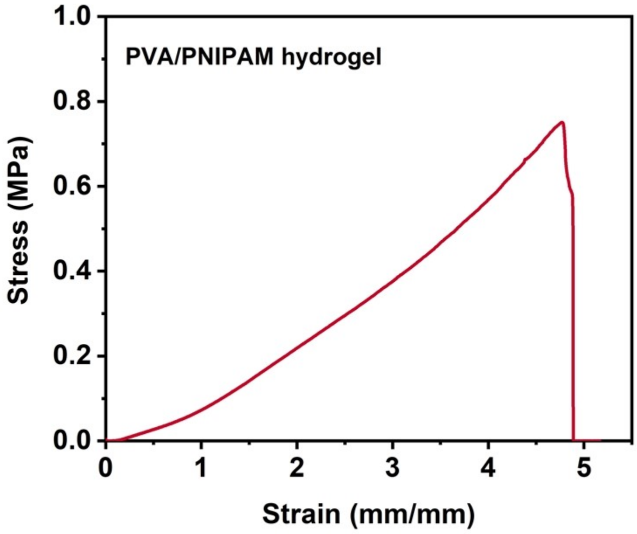

Figure S3. Stress-strain curve of PVA/PNIPAM hydrogel.

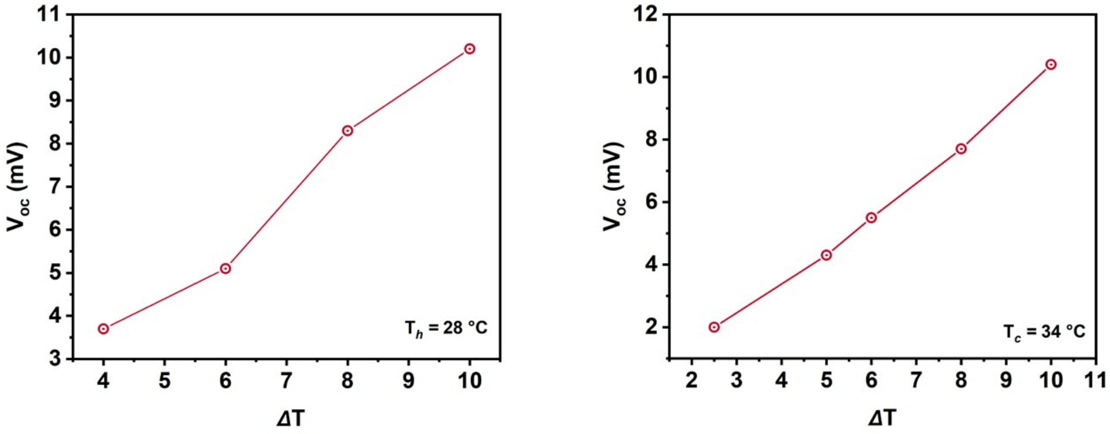

Figure S4. Thermovoltage–temperature relationship measured with the hot-side maximum temperature set to 28 °C (< LCST) and the cold-side temperature set to 34 °C (> LCST).

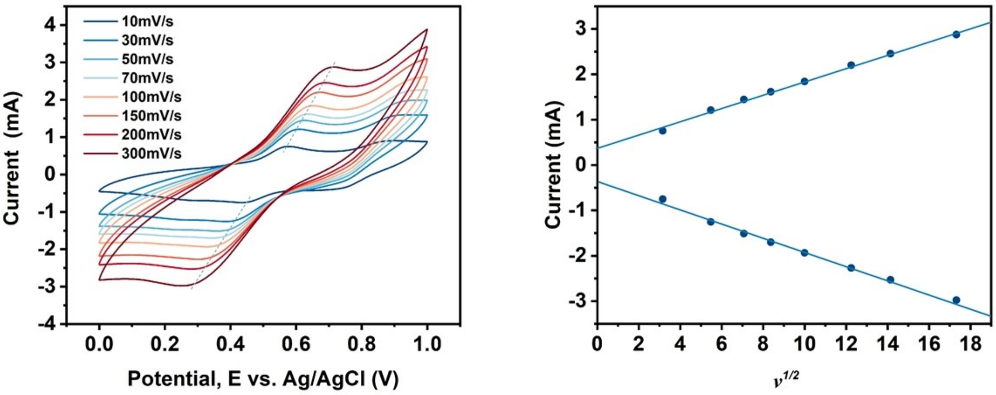

Figure S5. CV curves of a 0.25 mM I^-/ I_3^- + 40 mM GdmCl electrolyte solution at room temperature under various scan rate, and the linear fit between the peak current and the square root of the scan rate.

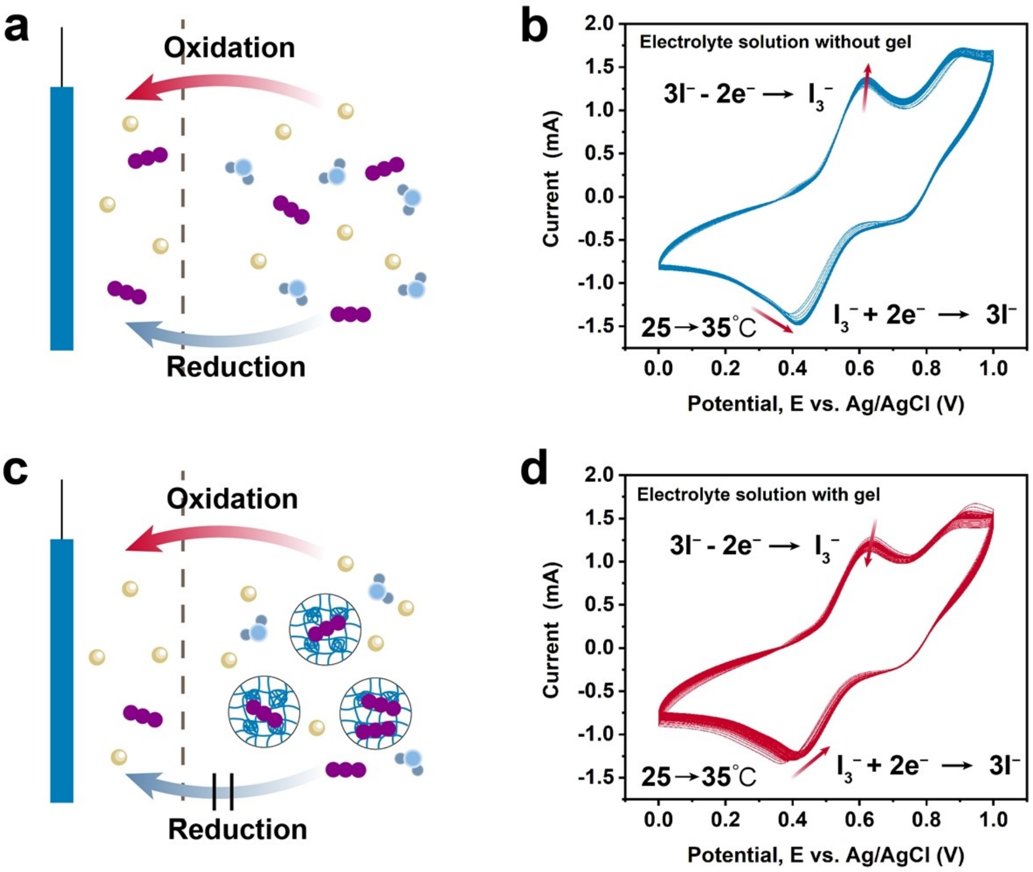

Figure S6. (a) Schematic illustration of the diffusion process of redox ions at the electrode–electrolyte interface in the absence of I_3^--adsorbing gel in the solution phase above LCST. (b) CV curves of the electrolyte solution without I_3^--adsorbing gel during heating from 25 °C to 35 °C. (c) Schematic illustration of the diffusion process of redox ions at the electrode–electrolyte interface in the presence of I_3^--adsorbing gel in the solution phase above LCST. (d) CV curves of the electrolyte solution containing I_3^--adsorbing gel during heating from 25 °C to 35 °C.

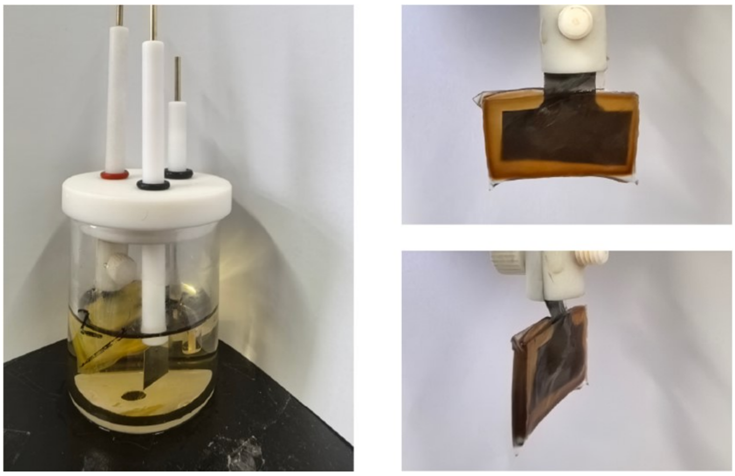

Figure S7. Three-electrode testing setup composed of a graphite electrode embedded in PVA/PNIPAM hydrogel.

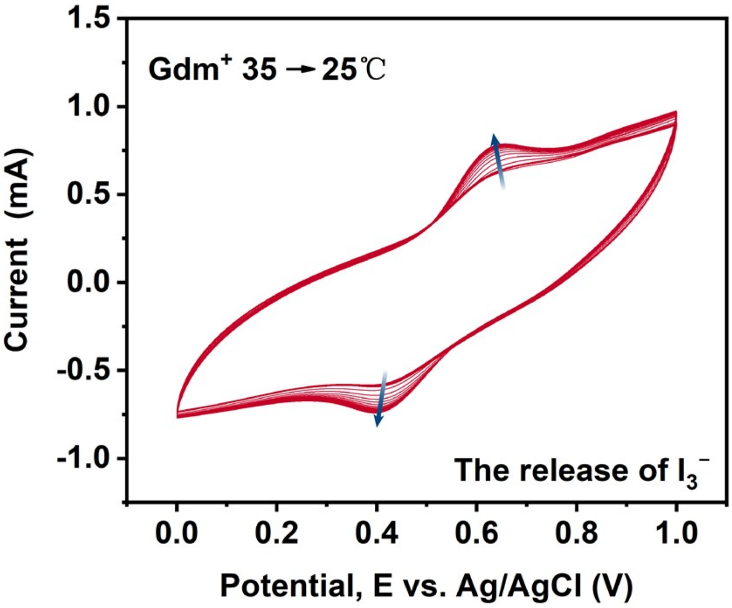

Figure S8. Evolution of CV curve in the gel containing Gdm$^+$ during the cooling process from 35 °C to 25 °C.

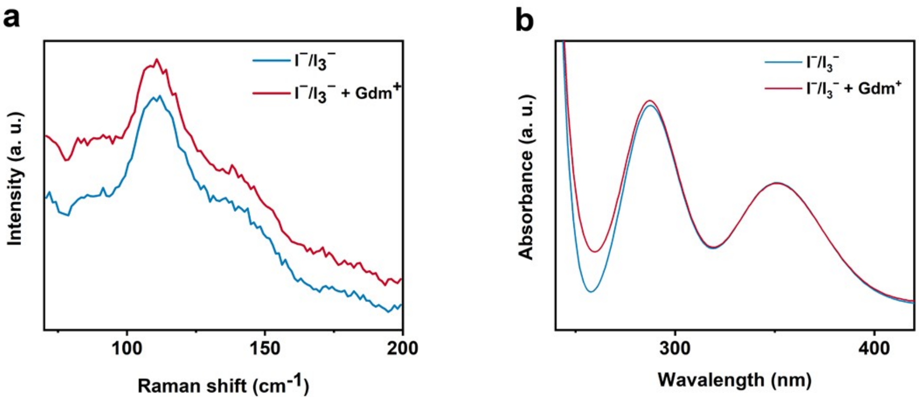

Figure S9. Raman (a) and UV-vis (b) spectra of I^-/ I_3^- solutions with and without Gdm^+.

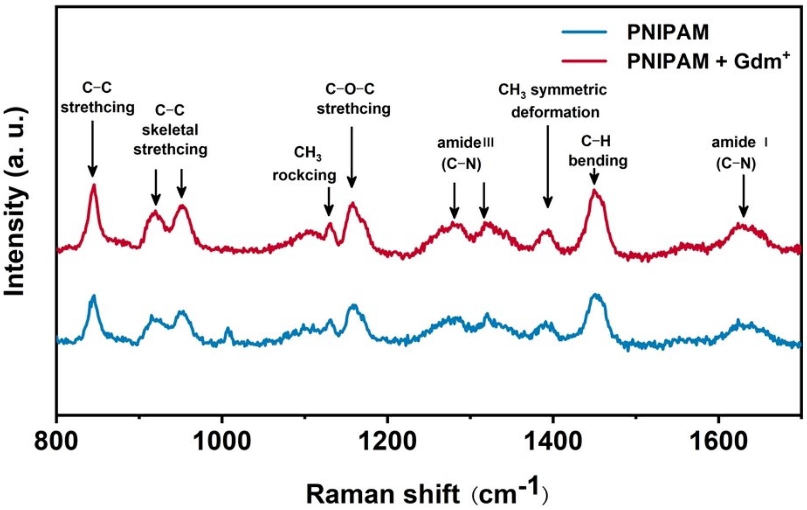

Figure S10. Raman spectra of PNIPAM hydrogels with and without Gdm^+.

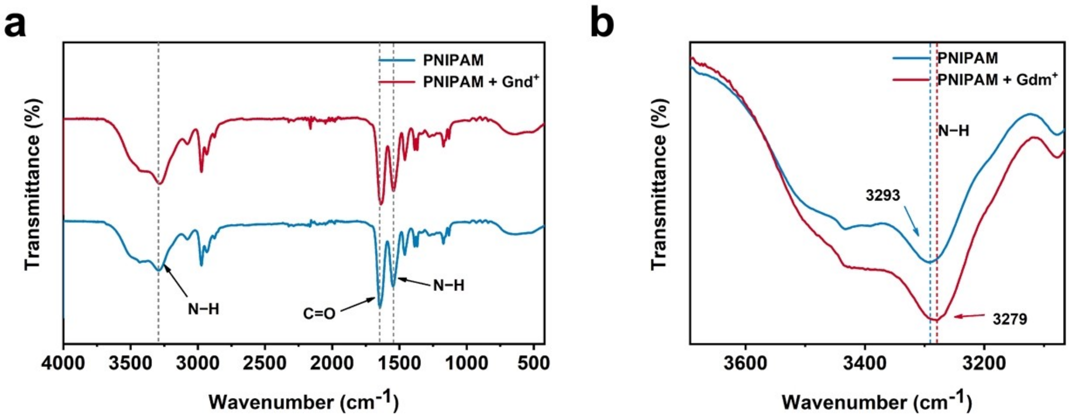

Figure S11. FTIR spectra of PNIPAM hydrogels with and without Gdm^+.

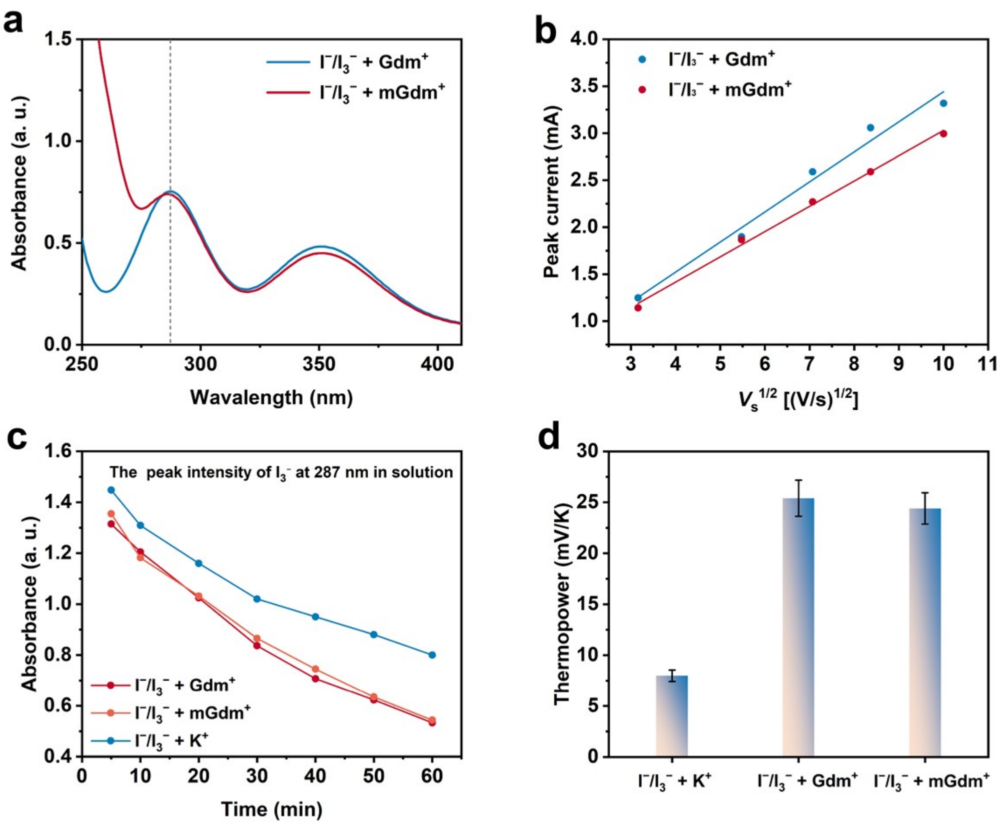

Figure S12. (a) UV–vis spectra of I^-/I_3^- solutions after the addition of Gdm^+ and $mGdm^+$. (b) Linear fitting of peak current versus the square root of scan rate for I^-/I_3^- solutions containing Gdm^+ and $mGdm^+$. (c) Changes in the UV–vis absorption peak of I_3^- at 287 nm in solution after PVA/PNIPAM hydrogel absorbed I_3^- above LCST, in the presence of 40 mM KCl, GdmCl, or mGdmCl. (d) Thermopower of TECs containing identical concentrations of K^+, Gdm^+, and $mGdm^+$.

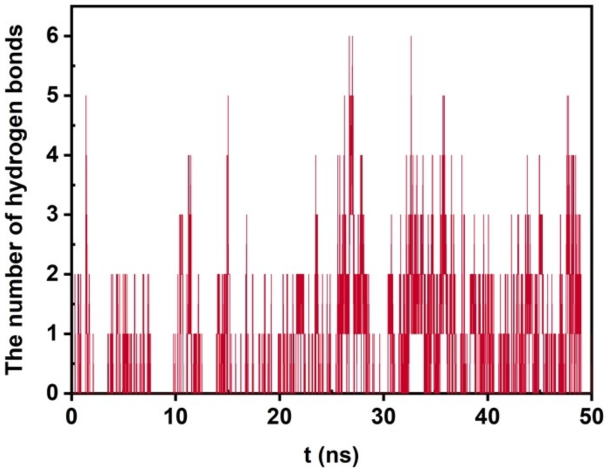

Figure S13. Number of hydrogen bonds formed between Gdm^+ and PNIPAM during molecular dynamics simulations.

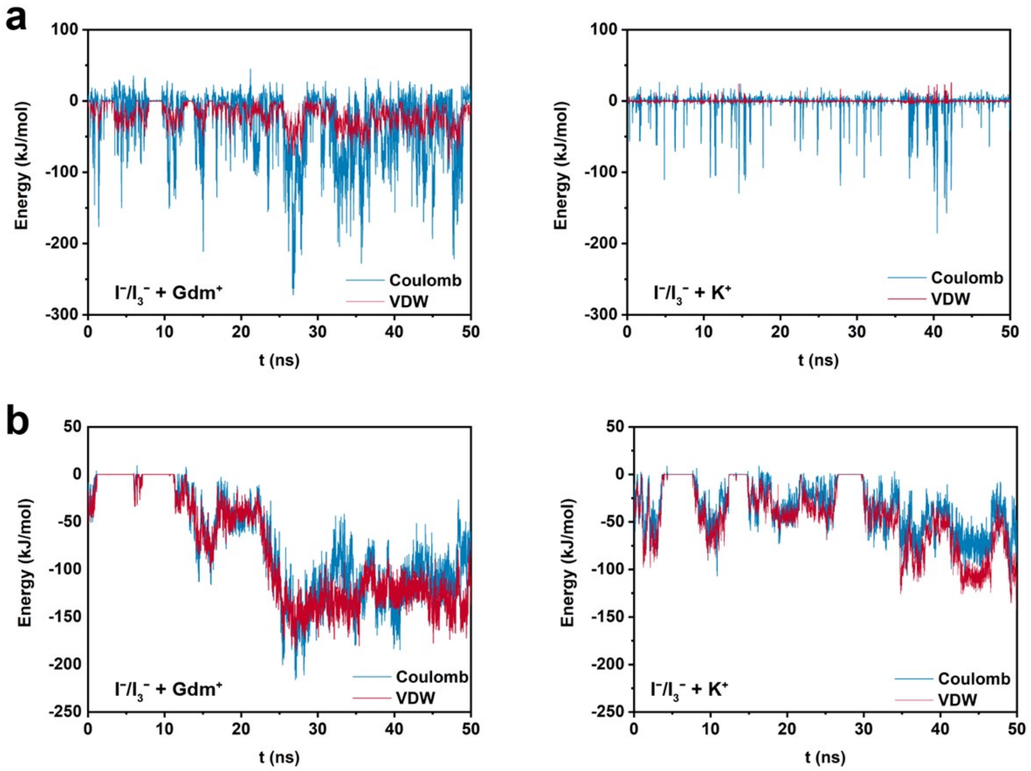

Figure S14. (a) Coulombic and van der Waals (VDW) interaction energy between Gdm^+ and PNIPAM, K^+ and PNIPAM chains obtained from molecular dynamics simulations. (b) Coulombic and VDW interaction energies between I_3^- and PNIPAM chains with Gdm^+ or K^+ obtained from molecular dynamics simulations.

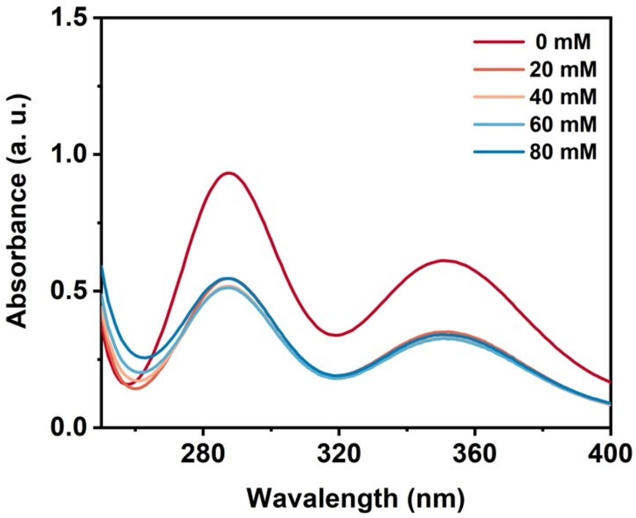

Figure S15. UV-vis spectra of I_3^- in electrolyte solutions with varying Gdm^+ concentrations above LCST, measured after absorption by the selective ion-adsorption hydrogel.

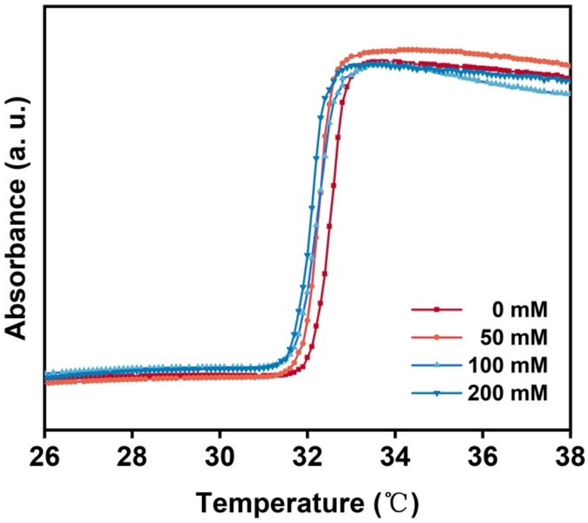

Figure S16. Solid-state UV–vis spectra of PVA/PNIPAM hydrogels containing varying concentrations of Gdm^+ during the heating process.

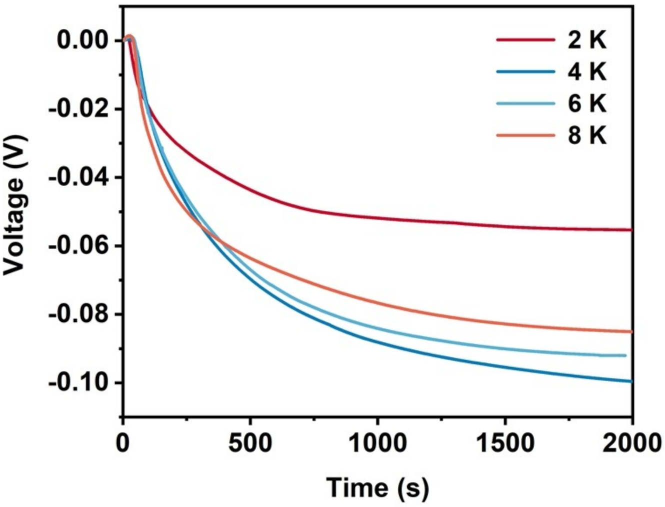

Figure S17. Open-circuit voltage–time curves of the TECs under different temperature difference.

Table S1. Comparison of thermopower between conventional TECs based on I^-/I_3^- system and

this work.

Redox couple	State	Matrix	Thermopower (| mV/K |)	References
I^-/I_3^-	Solution	Methylcellulose	9.62	8
	Solution	Cs^+	1.2	9
	Solution	poly (N-isopropylacrylamide)	1.91	10
	Solution	α-cyclodextrin	2.0	11
	Solution	Dimethyl carbonate	7.7	12
	Solution	Starch	1.5	13
	Gel	Methylcellulose	6.84	7
	Gel	Poly(methacrylic acid-co-3-dimethyl(methacryloyloxyethyl)ammonium propane sulfonate)	7.7	14
	Gel	poly(vinyl alcohol)-graft-α-cyclodextrin	14.24	15
	Gel	**poly (N-isopropylacrylamide)/ poly(vinyl alcohol)**	**25.4**	**This work**

References

1 B. Hess, GROMACS 4: Algorithms for highly efficient, load-balanced, and scalable molecular simulation. *Abstr. Pap. Am. Chem. Soc.*, **2009**, 4, 435-447.

2 R. B. Best, X. Zhu, J. Shim, P. E. M. Lopes, J. Mittal, M. Feig and A. D. MacKerell, Jr., Optimization of the Additive CHARMM All-Atom Protein Force Field Targeting Improved Sampling of the Backbone φ, ψ and Side-Chain χ_1 and χ_2 Dihedral Angles. *J. Chem. Theory Comput.*, **2012**, 8, 3257-3273.

3 U. Essmann, L. Perera, M. L. Berkowitz, T. Darden, H. Lee and L. G. Pedersen, A Smooth Particle Mesh Ewald Method. *J. Chem. Phys.*, **1995**, 103, 8577-8593.

4 B. Hess, H. Bekker, H. J. C. Berendsen and J. Fraaije, J. LINCS: A linear constraint solver for molecular simulations. *J. Comput. Chem.*, **1997**, 18, 1463-1472.

5 Y. Liu, M. Cui, W. Ling, L. Cheng, H. Lei, W. Li and Y. Huang, Thermo-electrochemical cells for heat to electricity conversion: from mechanisms, materials, strategies to applications. *Energy Environ. Sci.*, **2022**, 15, 3670-3687.

6 B. Yu, J. Duan, H. Cong, W. Xie, R. Liu, X. Zhuang, H. Wang, B. Qi, M. Xu, Z. L. Wang and J.

Zhou, Thermosensitive crystallization-boosted liquid thermocells for low-grade heat harvesting. *Science*, **2020**, 370, 342-346.

7 J. Li, S. Chen, X. Qu, Z. Han, Z. Zhou, L. Deng, Y. Jia, S. Zhang, R. Xie and H. Wang, Confined phase transition triggering a high-performance energy storage thermo-battery. *Energy Environ. Sci.*, **2024**, 17, 6606-6615.

8 Y. Han, J. Zhang, R. Hu and D. Xu, High-thermopower polarized electrolytes enabled by methylcellulose for low-grade heat harvesting. *Sci. Adv.*, **2022**, 8, eabl5318.

9 H. Wang, X. Zhuang, W. Xie, H. Jin, R. Liu, B. Yu, J. Duan, L. Huang and J. Zhou, Thermosensitive-CsI_3-crystal-driven high-power I^-/I_3^- thermocells. *Cell Rep. Phys. Sci.*, **2022**, 3, 100737.

10 J. Duan, B. Yu, K. Liu, J. Li, P. Yang, W. Xie, G. Xue, R. Liu, H. Wang and J. Zhou, P-N conversion in thermogalvanic cells induced by thermo-sensitive nanogels for body heat harvesting. *Nano Energy*, **2019**, 57, 473-479.

11 H. Zhou, T. Yamada and N. Kimizuka, Supramolecular Thermo-Electrochemical Cells: Enhanced Thermoelectric Performance by Host-Guest Complexation and Salt-Induced Crystallization. *J. Am. Chem. Soc.*, **2016**, 138, 10502-10507.

12 K. Kim, J. Kang and H. Lee, Hybrid thermoelectrochemical and concentration cells for harvesting low-grade waste heat. *Chem. Eng. J.*, **2021**, 426, 131797.

13 H. Zhou, T. Yamada and N. Kimizuka, Thermo-electrochemical cells empowered by selective inclusion of redox-active ions by polysaccharides. *Sustainable Energy & Fuels*, **2018**, 2, 472-478.

14 J. Shen, X. Huang, Y. Dai, X. Zhang and F. Xia, N-type and P-type series integrated hydrogel thermoelectric cells for low-grade heat harvesting. *Nat. Commun.*, **2024**, 15, 9035.

15 S. T. Kao, C. C. Hsu, S. H. Hong, U. S. Jeng, C. H. Wang, S. H. Tung and C. L. Liu, Host–Guest complexation of α-cyclodextrin and triiodide ions for enhanced performance of ionic thermoelectric capacitors. *Adv. Energy Mater.*, **2025**, 15, 2405502.